Chemical Science

ROYAL SOCIETY OF CHEMISTRY

EDGE ARTICLE

View Article Online
View Journal

Cite this: DOI: 10.1039/d5sc09241h

All publication charges for this article have been paid for by the Royal Society of Chemistry

Rational regulation of the torsion angle of covalent organic frameworks for enhanced CO_2 photoreduction to ethane

Yun Ma,[a] Qian Zhang,*[a] Hao Chen,[b] Huiyong Wang,*[a] Yunjing Deng,[a] Yingying Guo,[a] Shuaiqi Gao[a] and Jianji Wang*[a]

Received 26th November 2025
Accepted 24th April 2026

DOI: 10.1039/d5sc09241h

rsc.li/chemical-science

Light-driven CO_2 reduction to hydrocarbon fuels is a green and sustainable technology to alleviate global warming while producing high value-added chemicals. However, highly efficient production of ethane (C_2H_6) remains a great challenge due to insufficient electron deliverability and sluggish C–C coupling kinetics. Herein, a series of β-ketoenamine linked Tp-COFs-Mo with different torsion angles were designed and synthesized for the photocatalytic CO_2 reduction reaction to C_2H_6. It was disclosed that these Tp-COFs-Mo had identical structural active sites of Mo–N_3O, while different torsion angles significantly affected their photocatalytic performance. Significantly, TpPa-COF-Mo exhibited a remarkable C_2H_6 production rate of 262.6 μmol g^{-1} h^{-1} and a high C_2H_6 electron selectivity of 91.8%, which exceeds that of the most COF-, POP-, and MOF-based photocatalysts reported previously. Mechanism studies revealed that the smaller torsion angle of TpPa-COF-Mo led to electron accumulation within the layers and stronger electron capturing capacity of Mo sites, which improved separation and transfer of photogenerated electrons along the intralayer, enhanced *H adsorption, and reduced the energy barrier for the formation of *CHOCO intermediate species, thus promoting the efficient conversion of CO_2 to C_2H_6. This work opens a new pathway to design efficient COF catalysts by optimizing the torsion angle of COFs.

Introduction

The intensive utilization of fossil fuels has resulted in a significant increase in atmospheric CO_2 concentration, exacerbating the greenhouse effect and energy crisis.[1,2] Utilizing solar energy to convert CO_2 into value-added fuels, inspired by natural photosynthesis in green plants, is considered one of the green pathways to achieve carbon neutrality.[3–5] Compared with widely generated C_1 products (*e.g.*, CO, CH_4, and HCOOH),[6–8] two-carbon (C_2) fuels, such as ethane (C_2H_6), possess higher energy density and economic values.[9,10] However, the formation process of C_2H_6 involves the transfer of 14 electrons and complexed proton coupling steps, lower content of electron accumulated at the catalytic sites,[11] and a high thermodynamic energy barrier of the C–C coupling process, which results in both a low selectivity and production rate of C_2H_6.[12–14] To tackle this issue, the development of novel and highly efficient photocatalysts is critically important.

As a class of porous crystalline polymers, covalent organic frameworks (COFs) feature layered stacking structures, designable π-conjugated backbones,[15,16] high specific surface areas, tunable porosities, precise regulation of active site distribution, and favorable diffusion and adsorption of substrate molecules.[17,18] These unique properties render COFs a highly promising candidate for the photocatalytic reduction of CO_2 to C_2H_6. However, the high recombination rate of photogenerated electron–hole pairs coupled with low electron mobility are unavoidable in COFs, which leads to fewer available electrons for catalysis.[19] To improve the separation efficiency of photogenerated electron–hole pairs and facilitate the electron transport efficiency in the CO_2 photoreduction process, the electronic structure of COFs can usually be tuned by incorporating functionalized blocks, such as the conjugated molecular fragments and donor–acceptor units, or adjusting the polarity and electron delocalization degree of the linkage in the COFs.[20,21] Meanwhile, the rotation and distortion of covalent bonds (*e.g.*, C–C bonds and aryl linkages) within COF layers often induce spatial angular deviations, resulting in the generation of torsion angles. Distinct from stacking modes or interlayer spacing regulation, which primarily target interlayer orbital overlap, the torsion angle modulates the planarity of the

[a]*Collaborative Innovation Center of Henan Province for Green Manufacturing of Fine Chemicals, Key Laboratory of Green Chemical Media and Reactions, Ministry of Education (China), School of Chemistry and Chemical Engineering, Xinxiang, Henan 453007, P. R. China. E-mail: qianzhang@htu.edu.cn; hywang@htu.edu.cn; jwang@htu.edu.cn*

[b]*Xi'an University of Architecture and Technology, School of Chemistry and Chemical Engineering, Xi'an 710055, P. R. China*

intralayer skeleton and intralayer π-conjugation. This essentially dictates electron delocalization and charge transport behaviors, modifying the internal electron transport rate and, consequently, the electron enrichment at catalytically active sites.[22,23] However, there are few reports on the research in this area.

On the other hand, constructing single metal sites on the COFs can significantly enhance the adsorption capacity of CO_2, facilitate the separation efficiency of photogenerated electron–hole pairs, and accelerate the C–C coupling reaction of reaction intermediates to produce the C_2H_6 product due to the highly exposed active sites.[24] Compared with the other single metal atoms, a Mo atom with empty d-orbitals may receive much more electrons from the σ orbital of CO_2 molecules, while the electrons in the occupied d-orbitals of Mo can transfer to the empty π* orbitals of CO_2 molecules. Thus, an electronic acceptance-feedback mechanism is established between Mo and CO_2, which leads to the enhanced adsorption capacity of CO_2.[25–27] Furthermore, anchoring a Mo atom in the photocatalyst can broaden its absorption range of visible light and promote electron transfer and separation efficiency of electron–hole pairs.[28–30] Several studies have reported that the Mo atom is the active site for the C–C coupling in the photocatalytic CO_2 reduction reaction (CO_2RR). For example, Ye *et al.*[31] reported that the Mo-TpBpy-COF photocatalyst with MoN_2 sites could be used for the photocatalytic CO_2RR to C_2H_4, and the production rate and electron selectivity were 3.57 μmol g^{-1} h^{-1} and 42.92%, respectively. Wang *et al.*[32] claimed that Por-POP-Mo exhibited a production rate of 157.2 μmol g^{-1} h^{-1} and a selectivity of 49.4% for C_2H_6 under visible light. Obviously, the Mo atom is a promising active site in the photocatalytic CO_2RR to C_{2+} products.

Herein, we designed and synthesized a series of β-ketoenamine linked two-dimensional COFs with different torsion angles, which were then anchored with single Mo sites for efficient photocatalytic C_2H_6 production from CO_2. It was found that the coordination mode of Mo in Tp-COFs-Mo was Mo–N_3O, and the photocatalytic performance could be readily modulated by using the magnitude of the torsion angle of the COFs. Under visible light irradiation, the optimized TpPa-COF-Mo with the smallest torsion angle showed a remarkable CO_2 reduction performance, with a C_2H_6 production rate of 262.6 μmol g^{-1} h^{-1} and an electron selectivity of 91.8%. DFT calculations and *in situ* spectroscopic studies indicated that the Mo site was mainly responsible for the C–C coupling reaction, while the smaller torsion angle facilitated electron transport and the accumulation of electrons on the Mo site, improved the adsorption capacity of *H, and lowered the coupling energy barrier of *CHO–*CO at the Mo site, thereby boosting the selectivity and production rate of C_2H_6.

Results

Structure and the coordination environment of Tp-COFs-Mo

A series of β-ketoenamine-linked two-dimensional COFs were prepared using 2,4,6-trihydroxybenzene-1,3,5-tricarbaldehyde (Tp) and aniline, including *p*-phenylenediamine (Pa), 4,4′-biphenylenediamine (Bd), and 4,4″-diaminoterphenyl (Ta) through a solvothermal Schiff base condensation reaction. The as-synthesized Tp-COFs were named TpPa-COF, TpBd-COF and TpTa-COF, respectively. Then, the mixtures of 2,2′-bipyridine, $MoCl_5$, and COFs were refluxed under an Ar atmosphere at 95 °C for 24 hours to obtain Tp-COFs-Mo, as shown in Fig. 1. The specific synthetic protocols for the above Tp-COFs and Tp-COFs-Mo are described in the SI.

To describe the crystalline characteristics of Tp-COFs and Tp-COFs-Mo, the powder X-ray diffraction (PXRD) patterns were recorded and are shown in Fig. 2a, S1 and S2. It is clear that the PXRD patterns showed excellent agreement between experimental and simulated reflections, confirming the AA stacked crystal structure of the three Tp-COFs. The sharp diffraction peaks at 4.7°, 3.5° and 2.9° for TpPa-COF, TpBd-COF and TpTa-COF were ascribed to the respective (100) crystal plane, which demonstrates high crystallinity.[33–35] Importantly, the characteristic peaks of the (001) crystal plane generated by the π-stacking in two-dimensional layers of TpPa-COF exhibited the largest 2θ value, indicating that its interlayer stacking distance is smaller than that of TpBd-COF and TpTa-COF,[36] which is consistent with the result obtained from refined unit-cell parameters using theoretical structural simulation calculations (Fig. 2a and S1). Furthermore, no diffraction peaks of molybdenum nanoparticles or molybdenum oxides were observed in the PXRD patterns of Tp-COFs-Mo, suggesting that molybdenum was present in the form of a coordinated structure in the Tp-COF matrix.[37] The torsion angles of the pristine Tp-COFs were first estimated using Materials Studio based on the experimental PXRD patterns. The obtained torsion angles were 12.3°, 32.3°, and 47.4° for TpPa-COF, TpBd-COF, and TpTa-COF, respectively (Fig. S3a–c). After Mo incorporation, the corresponding torsion angles were determined to be 12.7°, 33.0°, and 48.5° for TpPa-COF-Mo, TpBd-COF-Mo, and TpTa-COF-Mo, respectively (Fig. S3d–f). The change in torsion angle induced by Mo introduction was only 0.4°, 0.7°, and 1.1°, indicating that Mo incorporation had quite a small influence on the framework torsion angle of Tp-COFs. To further support this structural feature, density functional theory (DFT) calculations were performed on the most stable structures, and the torsion angles were determined from four adjacent atoms in the framework. The calculated torsion angles of TpPa-COF-Mo, TpBd-COF-Mo, and TpTa-COF-Mo were 11.1°, 30.0°, and 45.3°, respectively (Fig. S4). Considering the fact that torsion angles obtained from DFT-optimized structures of similar COFs reported in different literature studies can differ by more than 4°,[38,39] the deviation between the experimental fitting values and DFT result observed here could be regarded as reasonable. These results consistently demonstrate that the framework torsion angle increased from TpPa-COF, TpBd-COF to TpTa-COF, while Mo incorporation did not significantly alter the intrinsic torsional geometry of the COF skeleton.

Interestingly, it was found that among the COF catalysts investigated in this work, TpPa-COF-Mo exhibited the smallest torsion angle and shortest interlayer stacking distance. This suggests that the variation in the torsion angle of the building block can result in a change in the interlayer stacking distance

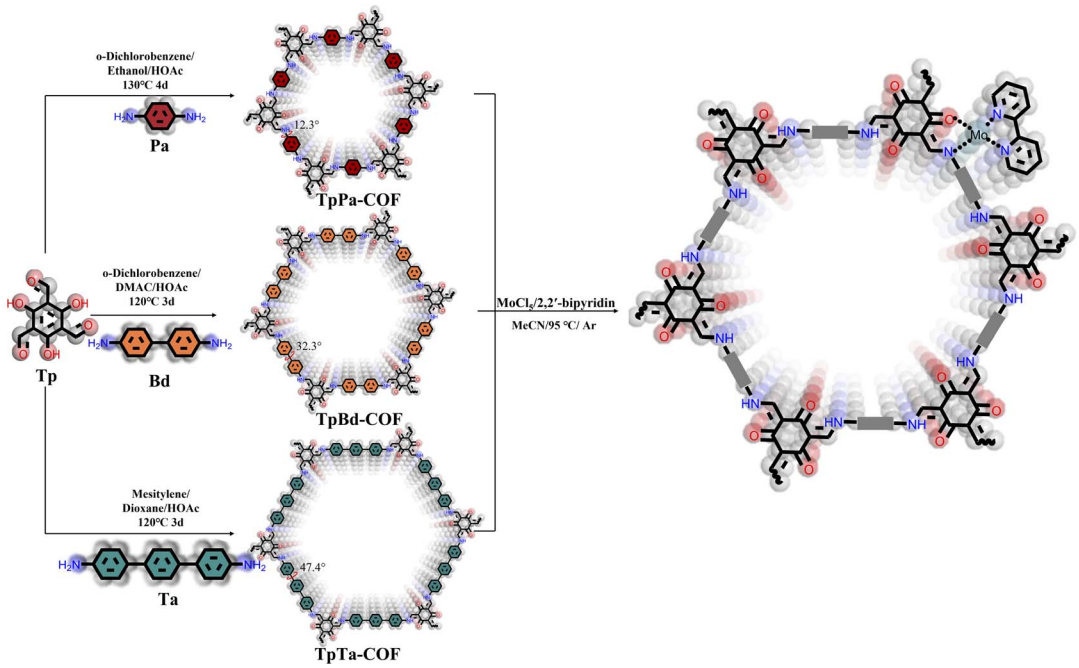

Fig. 1 Schematic diagram for the synthesis of β-ketoenamine-linked Tp-COFs-Mo.

in the COFs. Furthermore, the charge density difference (CDD) in the bilayer structures of the COFs was analyzed to elucidate the impact of interlayer interactions on electron transport. Specifically, compared with TpBd-COF and TpTa-COF, distinct electron depletion was observed in the interlayer region of TpPa-COF, while electron accumulation was concentrated on the intralayer β-ketoenamine groups and aromatic rings (Fig. S5).

While the smaller torsion angle of TpPa-COF creates a more planar backbone and tighter stacking (interlayer distance of 3.2 Å), this extremely close proximity induces strong Pauli repulsion between the filled π-electron clouds of adjacent layers.[40] This repulsion effectively weakens the effective interlayer electronic coupling, and prevents charge delocalization across the layers, thereby facilitating efficient electron transport along the intralayer framework.[41]

Using Fourier transform infrared (FTIR) spectra of TpPa-COF and its precursor modules as an example (Fig. 2b), we observed new vibration absorption peaks at 1575 cm^{-1} (C═C), 1220 cm^{-1} (C–N), and 1602 cm^{-1} (C═O), along with the disappearance of the amino bond (–NH_2) in Pa at ~3196–3371 cm^{-1} and aldehyde (–CHO) in Tp at 1635 cm^{-1},[42] which suggested the formation of a β-ketoenamine structure in TpPa-COF through enol-to-keto tautomerism.[43,44] After anchoring a Mo atom into TpPa-COF, the peaks of C–N (1256 cm^{-1}) and C═O (1608 cm^{-1}) showed a blueshift, indicating the Mo coordination with O and N atoms of the β-ketoenamine group in TpPa-COF. Moreover, the FTIR spectra of TpBd-COF-Mo and TpTa-COF-Mo also exhibited a similar trend (Fig. S6). The obtained BET specific surface area through N_2 adsorption isotherms at 77 K was 805.0, 1180.1 and 545.9 $m^2\ g^{-1}$ for TpPa-COF, TpBd-COF, and TpTa-COF, respectively (Fig. S7). The BET specific surface area of TpTa-COF sharply decreased compared to that of the other COFs, due to the larger torsion angle of the Ta building block, which exacerbates the interpenetration and entanglement of the COF framework.[42] Additionally, the specific surface area of TpPa-COF-Mo, TpBd-COF-Mo and TpTa-COF-Mo was 193.1, 213.3, and 384.2 $m^2\ g^{-1}$, respectively. Their pore sizes were 1.27, 1.67, and 2.05 nm, which were smaller than those of the corresponding parent COF (1.67, 2.12, and 2.52 nm for TpPa-COF, TpBd-COF, and TpTa-COF). Obviously, the introduction of Mo into the COFs decreased the surface area and pore size owing to partial occupation of Mo atoms in the pore channels of COFs.

Thermogravimetric analysis (TGA) curves of Tp-COFs and Tp-COFs-Mo indicated that they were thermally stable up to 300 °C (Fig. S8). Scanning electron microscopy (SEM) images showed that Tp-COFs-Mo maintained a similar ribbon-like morphology after the introduction of Mo ions (Fig. S9). Furthermore, the high-resolution transmission electron microscopy (HR-TEM) images of TpPa-COF-Mo displayed an interlayer spacing of 0.33 nm along the *c* direction and a hexagonal pore diameter of 1.23 nm (Fig. 2c and S10), which were in agreement with the results from PXRD. Energy dispersive X-ray (EDX) mappings demonstrated that Mo was uniformly distributed in the TpPa-COF framework without any clustering (Fig. S11). The Mo content in Tp-COFs-Mo was evaluated by inductively coupled plasma mass spectrometry (ICP-MS) to be 15.0 wt%, 15.7 wt% and 15.3 wt% for TpPa-COF-Mo, TpBd-COF-Mo and TpTa-COF-Mo, respectively (Table S1).

To characterize the valence state and coordination surroundings of Mo in TpPa-COF-Mo, X-ray photoelectron spectroscopy (XPS), Fourier transformed extended X-ray absorption fine structure (FT-EXAFS), and X-ray absorption near-edge structure (XANES) analysis were employed. As shown

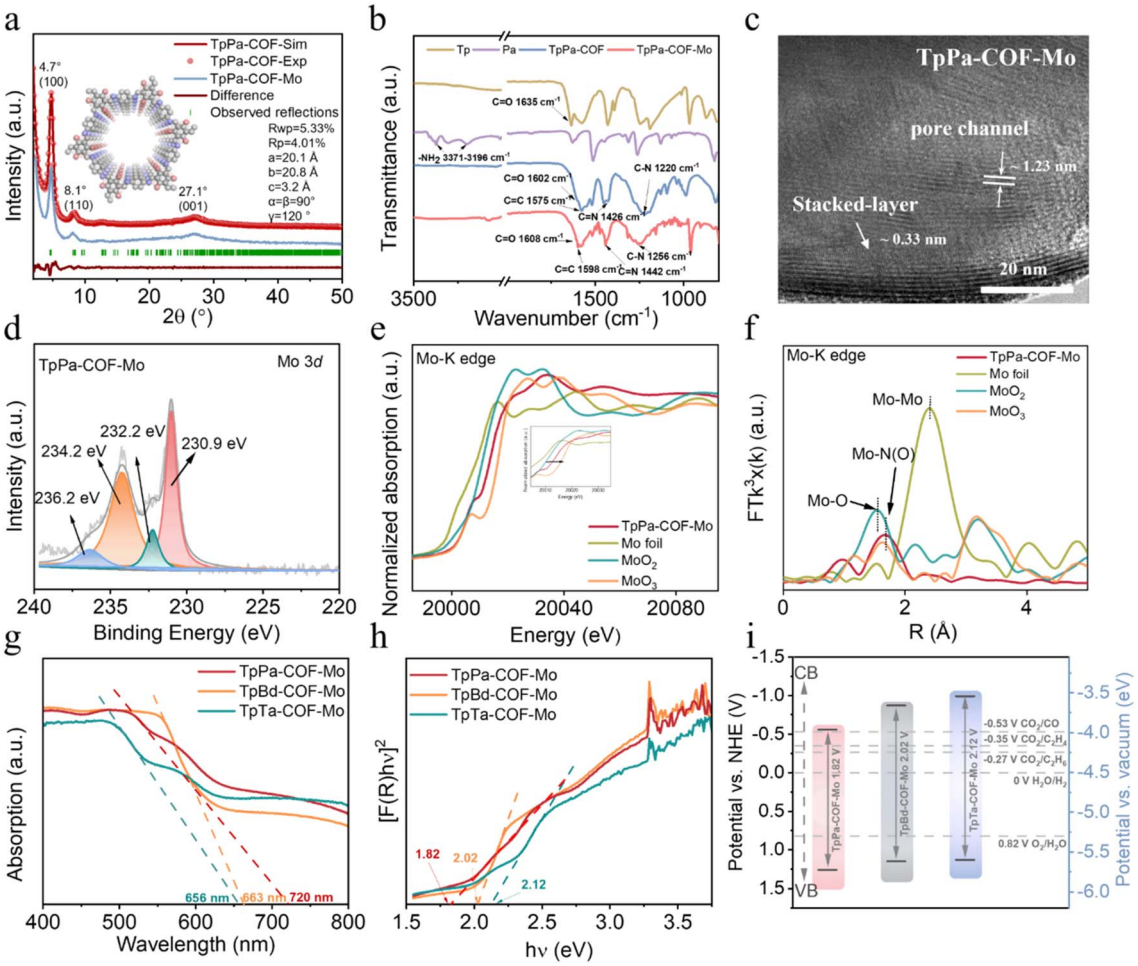

Fig. 2 Structure characterization. (a) X-ray diffraction (XRD) patterns and (b) FTIR spectra of TpPa-COF and TpPa-COF-Mo. (c) TEM images of TpPa-COF-Mo. (d) High-resolution XPS spectra of Mo 3d for TpPa-COF-Mo. (e and f) Normalized XANES and FT-EXAFS spectra at the Mo K-edge of TpPa-COF-Mo, Mo foil, MoO_2, and MoO_3 samples. (g) UV-vis diffuse reflection spectra of Tp-COFs-Mo. (h) Kubelka–Munk transformed spectra of Tp-COFs-Mo. (i) Schematic band structure diagram of Tp-COFs-Mo.

in Fig. 2d, the Mo $3d_{5/2}$ peak in the XPS spectrum of TpPa-COF-Mo could be resolved into two peaks at 230.9 and 232.2 eV, and the Mo $3d_{3/2}$ peak could be also deconvoluted into two peaks at 234.2 and 236.2 eV, demonstrating that Mo in TpPa-COF-Mo mainly existed in +5 along with a small amount of +6 oxidation state,[45,46] stemming from the oxidization of a small number of Mo^{5+} by air during the material synthesis process. The same conclusion was derived from the XPS spectrum of TpBd-COF-Mo and TpTa-COF-Mo (Fig. S12). In addition, the N 1s spectrum of 2,2′-bipyridine exhibited a pyridine-N peak at 398.7 eV and TpPa-COF exhibited C=N and C–N peaks at 399.6 and 401.1 eV (Fig. S13). The pyridine-N, C=N and C–N peaks showed consistent binding energy shifts as well as the appearance of a new Mo–N peak at 397.3 eV, indicating that the Mo ion was coordinated with N atoms of the 2,2′-bipyridine and β-ketoenamine linkage in TpPa-COF-Mo. The O 1s spectrum of TpPa-COF could also be resolved into C–O–H (531.9 eV) and C=O (533 eV). Compared with TpPa-COF, the peak shift of both C–O–H (from 531.9 to 531.7 eV) and C=O (from 533 to 532.8 eV) and appearance of a new Mo–O peak (533.6 eV) in TpPa-COF-Mo suggested that Mo was bonded by O atoms of the β-ketoenamine linkage in the COF. A similar result was found for TpBd-COF-Mo and TpTa-COF-Mo (Fig. S14).

Fig. 2e exhibits XANES spectra at the Mo K-edge for TpPa-COF-Mo, Mo foil, MoO_2 and MoO_3 samples. The near absorption edge of TpPa-COF-Mo was positioned between that of MoO_2 and MoO_3 and close to that of MoO_3, which indicates that the valence state of Mo in TpPa-COF-Mo was between +5 and +6, which was consistent with the XPS result. Furthermore, it can be seen from Fig. 2f that in the EXAFS spectrum at the Mo K-edge of TpPa-COF-Mo, the primary peak of the first coordination shell for Mo was at 1.66 Å, close to the Mo–O peak at 1.56 Å for MoO_2 and MoO_3, implying the presence of Mo–N or Mo–O bonds in TpPa-COF-Mo. However, no Mo–Mo peak at 2.4 Å was observed, which suggests the existence of the atomically dispersed Mo site and the absence of Mo clusters or nanoparticles in TpPa-COF-Mo.[47] The wavelet transform (WT) image was used to further ascertain the atomic dispersion of Mo in TpPa-COF-Mo *via* comparison with the standard sample (Fig. S15). The ordinate of the main peak in the TpPa-COF-Mo contour plot was located at approximately 1.66 Å, which was ascribed to the

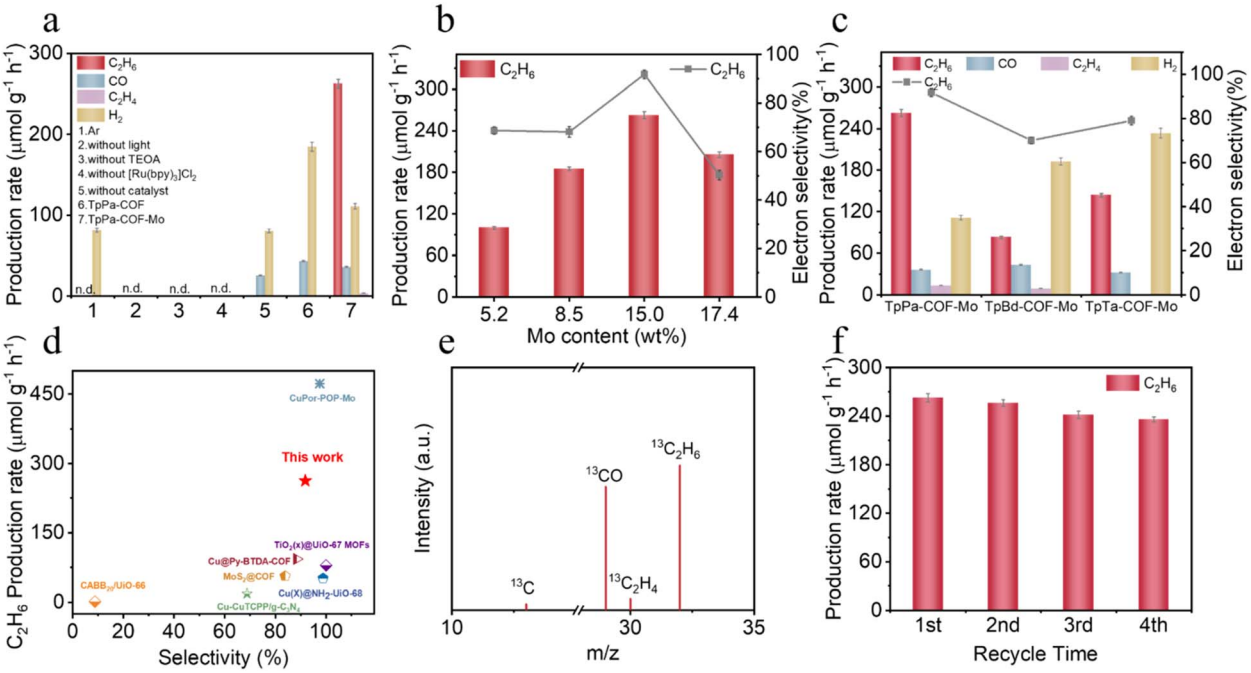

Fig. 3 Optimization of the catalytic conditions using TpPa-COF-Mo as the catalyst. (a) Control experiments under different photocatalytic conditions for TpPa-COF-Mo. (b) Catalytic production of C_2H_6 over TpPa-COF-Mo with different Mo loadings. (c) Comparison of the photocatalytic CO_2 reduction performance for different Tp-COFs-Mo. (d) Comparison of the production rate of C_2H_6 using TpPa-COF-Mo as a photocatalyst with porous materials reported in recent literature. (e) Gas chromatography-mass spectrometry in ^{13}C isotope tracer tests. (f) The production rate of C_2H_6 for each cycle of TpPa-COF-Mo as the photocatalyst.

Mo–N(O) coordination. In addition, no maximum intensity of the Mo–Mo bond was observed in the second shell at approximately 2.4 Å, providing additional evidence for the absence of the Mo–Mo bond in TpPa-COF-Mo. The specific coordination number and local microenvironment surrounding the Mo centre were explored *via* the fitting of EXAFS data to the first coordination shell of TpPa-COF-Mo (Fig. S16 and Table S2). The fitting results indicated that each Mo ion coordinates with four atoms, featuring Mo–N bonds in the range of 1.94–2.08 Å and a Mo–O bond at 2.12 Å. Combined with the FT-IR and the XPS spectral results, the Mo–N_3O coordination in TpPa-COF-Mo was formed by one nitrogen and one oxygen atom of the β-ketoenamine linkage, as well as the two nitrogen atoms in 2,2′-bipyridine (Fig. S18a). Furthermore, the XAFS measurements for TpBd-COF-Mo and TpTa-COF-Mo reveal identical oxidation states and coordination geometries (Mo–N_3O) to those of TpPa-COF-Mo (Fig. S17, S18b, c, and Table S2).

Optical characters and photocatalytic performance

The optical absorption characteristics and band gap of Tp-COFs and Tp-COFs-Mo were measured using UV-vis diffuse reflectance spectroscopy. It was found that TpPa-COF-Mo exhibited the longest absorption edge and the narrowest optical band gap (E_g) of 1.82 eV, which is more favorable for electron transfer from the valence band (VB) to the conduction band (CB) (Fig. 2g, h and S19). Mott–Schottky plots indicate that the COFs are n-type semiconductors, and the CB and VB values of TpPa-COF-Mo at pH = 7 were −0.76 and 1.26 eV *vs.* the normal hydrogen electrode (NHE), respectively (Fig. S20). Based on the band structure, it can be seen that the photoinduced electrons generated from $[Ru(bpy)_3]Cl_2$ are more conducive to transfer to TpPa-COF-Mo,[48] and the CO_2 photoreduction process was thermodynamically favorable (Fig. 2i and S21).

Encouraged by the above results, the photocatalytic CO_2RR by Tp-COFs-Mo was conducted in a mixed solution of acetonitrile and water under visible light irradiation (λ = 420–780 nm) by using $[Ru(bpy)_3]Cl_2$ and triethanolamine (TEOA) as the photosensitizer and electron donor, respectively. Taking TpPa-COF-Mo as an example, a series of control tests were performed, and the results are shown in Fig. 3a. It was noticeable that in the presence of TpPa-COF-Mo, C_2H_6 was the main product, as determined by gas chromatography (GC) (Fig. S22), and no liquid phase products were observed by ^1H NMR spectroscopy (Fig. S23). Similarly, for TpBd-COF-Mo and TpTa-COF-Mo catalysts, C_2H_6 was also the main product. However, for TpPa-COF without Mo, only small amounts of H_2 and CO were detected (Fig. S24). The CO production rate over pristine Tp-COFs increased in the order TpPa-COF > TpTa-COF > TpBd-COF (Fig. S25). These results indicated that in the Tp-COFs-Mo photocatalyst, the Mo site was pivotal for the production of C_2H_6 through the C–C coupling reaction, which achieved our expected design goal. Subsequently, to achieve excellent yield and selectivity of C_2H_6, the reaction conditions (volume ratio of acetonitrile/water, dosage of the catalyst, irradiation time, and content of Mo in Tp-COFs-Mo) were optimized for the photocatalytic CO_2RR under TpPa-COF-Mo catalysis.

It was noted from Fig. S26–28 and 3b that when the volume ratio of acetonitrile/water was 49 : 1, the dosage of TpPa-COF-

Mo was 2 mg, irradiation time was 2 h, and content of Mo was 15.0 wt%, the highest production rate and selectivity of C_2H_6 were obtained. Furthermore, as shown in Fig. 3b and S29, the photocatalytic performance and electron selectivity exhibited continuous improvement with the increase in Mo loading from 5.2 wt% to 15.0 wt%, which was attributed to the enhanced density of well-dispersed Mo active sites within the TpPa-COF-Mo framework. However, when the Mo loading was further increased to 17.4 wt%, slight aggregation of Mo was observed, which reduces the number of atomically dispersed Mo active sites and impedes mass transfer within the porous channels, thereby resulting in the reduction of catalytic performance and electron selectivity.[49] Under the optimized conditions, both the production rate and electron selectivity of C_2H_6 over TpPa-COF-Mo reached 262.6 μmol g^{-1} h^{-1} and 91.8%, respectively. Thus, the C_2H_6 production rate of TpPa-COF-Mo is 3.2 and 1.8 times that of TpBd-COF-Mo (82.6 μmol g^{-1} h^{-1}) and TpTa-COF-Mo (143.7 μmol g^{-1} h^{-1}), respectively. Concurrently, the electron selectivity of C_2H_6 over TpPa-COF-Mo was much higher than that of TpBd-COF-Mo (70.1%) and TpTa-COF-Mo (79.1%). Obviously, the smallest torsion angle in TpPa-COF-Mo induced strong Pauli repulsion, and significantly promoted electron transfer and accumulation at the Mo sites, thus endowing it with the highest C_2H_6 selectivity and production rate compared with TpBd-COF-Mo and TpTa-COF-Mo. Although TpBd-COF-Mo possesses a moderate torsion angle, it neither has the efficient intralayer electron transport promoted by interlayer Pauli repulsion as in TpPa-COF-Mo, nor possesses the continuous π-conjugated network as in TpTa-COF-Mo to compensate for the insufficient planarity of the framework. Owing to the weaker electron transfer in TpBd-COF-Mo, the charge accumulation on the Mo active sites is the lowest, resulting in the poorest catalytic selectivity and C_2H_6 production rate. To the best of our knowledge, the production rate, selectivity and TOF of C_2H_6 reported here exceeded those of most of the previously reported metal–organic framework (MOF)-, porous organic polymer (POP)-, and COF-based photocatalysts under broadly comparable conditions (Fig. 3d and Table S3). To confirm the carbon origin of C_2H_6, the CO_2RR experiment using $^{13}CO_2$ as the substrate was performed (Fig. 3e). The major signals with m/z values of 13, 29, 30 and 32 assigned to ^{13}C, ^{13}CO, $^{13}C_2H_4$ and $^{13}C_2H_6$, respectively, were detected by gas chromatography-mass spectrometry, which confirms that the generated C_2H_6 originated from CO_2 rather than other organic species. The apparent quantum efficiency (AQE) for photocatalytic CO_2 to ethane over TpPa-COF-Mo was investigated at different wavelengths and the highest AQE value was 0.15% detected at 450 nm, which is higher than that of the most reported COF-based photocatalysts in a similar situation (Fig. S30 and Table S5). The stability of photocatalysts was also evaluated. As shown in Fig. 3f, the production rate of C_2H_6 over TpPa-COF-Mo exhibited no significant decrease after the fourth cycle of the photoreaction, indicating that the photocatalyst demonstrated good stability. Moreover, XRD, FTIR, SEM and XPS characterization studies conducted before and after the fourth cycle of the photocatalytic CO_2RR indicate the structural integrity of the TpPa-COF-Mo catalyst, with a well-maintained Mo–N_3O coordination environment (Fig. S31). To determine whether Mo in the catalyst was leached into the liquid phase during the long-term photocatalytic reaction, we analyzed the Mo content in the liquid phase during the long-term photocatalytic reaction over 50 h using inductively coupled plasma optical emission spectrometry (ICP-OES). It was indicated that approximately 9.7% of the loaded Mo leached into the reaction solution.

Possible reaction mechanism

To clarify the causes of the superior performance of TpPa-COF-Mo, the photogenerated electron transfer and photogenerated electron–hole separation efficiency were first investigated. Compared with TpBd-COF-Mo and TpTa-COF-Mo, TpPa-COF-Mo showed a higher transient photoelectric current intensity and a smaller semicircle in Nyquist plots, implying that the smaller torsion angle of the COF could improve the separation efficiency of photo-generated electron–hole pairs and transfer rate of photo-generated electrons (Fig. S32). This result was further supported by the lowest emission spectral intensity and a much longer fluorescence lifetime (τ_{avg} = 2.58 ns) of TpPa-COF-Mo obtained from the steady-state PL spectra (Fig. S33). The steady-state PL spectra of the mixture with Tp-COFs-Mo and $[Ru(bpy)_3]Cl_2$ illustrated that Tp-COFs-Mo could quench the emission of $[Ru(bpy)_3]Cl_2$, and TpPa-COF-Mo displayed the most significant PL quenching effect, resulting in a shorter electron excitation lifetime of $[Ru(bpy)_3]Cl_2$ (150.4 ns) (Fig. S34). This result revealed that the recombination of photo-generated electron–hole pairs of $[Ru(bpy)_3]Cl_2$ was better inhibited by TpPa-COF-Mo, and long-lived electrons were provided for CO_2 reduction, leading to enhanced CO_2 photo-reduction efficiency. Overall, the smaller torsion angle in TpPa-COF-Mo effectively promoted intralayer electron migration and transport, and significantly suppressed the recombination of photogenerated electron–hole pairs.

Moreover, the exciton dissociation kinetics is a key parameter for quantifying the Coulomb interaction between photogenerated electrons and holes.[50] Therefore, the exciton binding energy (E_b) of Tp-COFs-Mo was obtained through temperature-dependent PL spectra, where the E_b value can be experimentally determined by fitting the PL peak intensity (I) at different temperatures to the Arrhenius equation: $I(T) = I_0/(1 + A\exp(-E_b/k_BT))$.[51] As shown in Fig. 4a and b, as the temperature was elevated from 80 to 300 K, the E_b value of Tp-COFs-Mo decreased in the order TpBd-COF-Mo (57.87 meV) > TpTa-COF-Mo (53.22 meV) > TpPa-COF-Mo (45.03 meV), indicating that the separation of photo-generated electron–hole pairs in TpPa-COF-Mo became easier compared to TpBd-COF-Mo and TpTa-COF-Mo.[52–54] Furthermore, femtosecond transient absorption (fs-TA) spectroscopy reveals that TpPa-COF-Mo features the fastest exciton transfer kinetics (τ_1 = 0.71 ps) and the longest carrier lifetime (τ_2 = 2175.21 ps), suggesting that intralayer charge transport is highly efficient and recombination is effectively suppressed (Fig. S35).[55] Based on the above results, TpPa-COF-Mo exhibited the highest photogenerated electron–hole separation efficiency and the fastest electron transport speed. Its smaller torsion angle minimized the

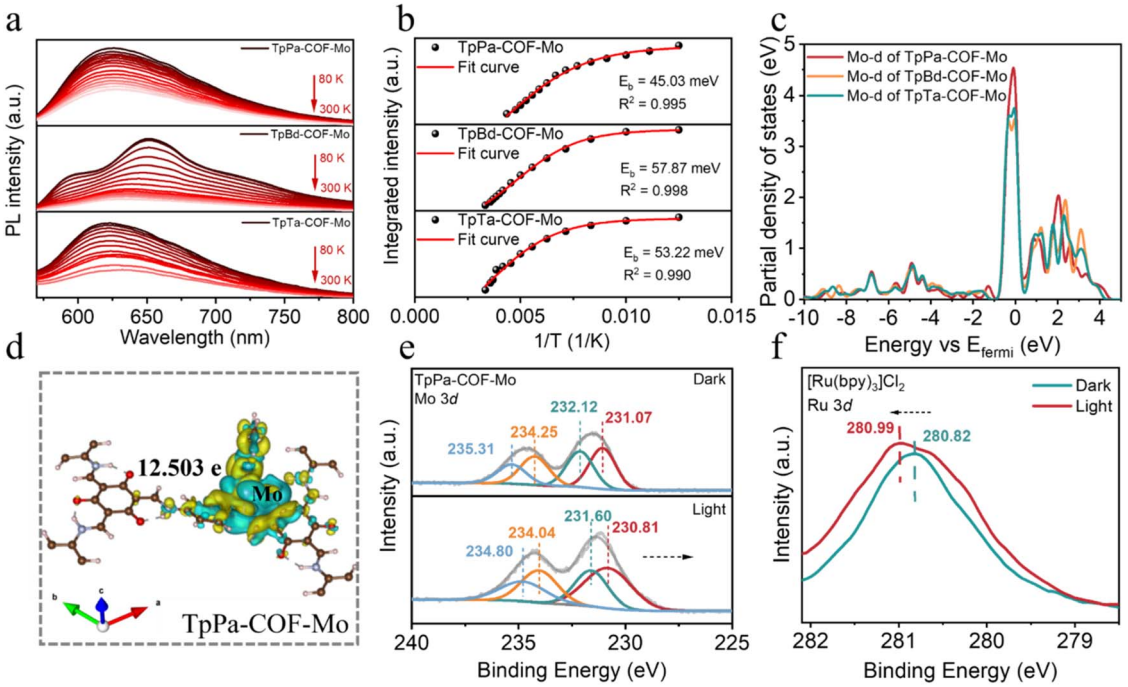

Fig. 4 Electron transfer of Tp-COFs-Mo. (a) Temperature-dependent PL spectrum of Tp-COFs-Mo excited at 450 nm. (b) Integrated PL emission intensity of Tp-COFs-Mo as a function of temperature. (c) The partial density of states (PDOS) of the Mo d-orbitals in Tp-COFs-Mo. (d) Isosurfaces (level 0.0002 eV Å^{-3}) of charge density differences of TpPa-COF-Mo. (e and f) Quasi-*in situ* XPS spectra of Mo 3d of TpPa-COF-Mo and Ru 3d of $[Ru(bpy)_3]Cl_2$ under light and in the dark.

interlayer distance, leading to strong Pauli repulsion that suppressed the relatively slow interlayer charge transfer and promoted efficient and rapid intralayer electronic flow.[53,56] Therefore, we can regulate the torsion angle of the COFs to effectively reduce the spatial hindrance of intralayer π-electron delocalization within the intralayer and promote the formation of continuous π-electron channels, thus improving the separation and transfer efficiency of photogenerated charges, and inhibiting reverse charge recombination.

The electronic density of the Mo catalytic site in Tp-COFs-Mo is very important for its C–C coupling ability. Therefore, the partial density of states (PDOS) diagram of the Mo d-orbital in Tp-COFs-Mo was calculated by DFT (Fig. 4c). It was found that the PDOS peak intensity of the Mo-d orbital at the Fermi level (E_f) in TpPa-COF-Mo was significantly higher than that of TpBd-COF-Mo and TpTa-COF-Mo, implying that TpPa-COF-Mo with the smallest torsion angle enhanced electronic density of the Mo site. The calculated Bader charge value for the Mo atom in TpPa-COF-Mo was 12.503*e* (Fig. 4d), while the value of the Mo atom in TpBd-COF-Mo and TpTa-COF-Mo was 12.435*e* and 12.455*e*, respectively (Fig. S36). These results also confirmed that the electronic density of Mo in TpPa-COF-Mo was higher than that of the other Tp-COFs-Mo. Additionally, quasi-*in situ* X-ray photoelectron spectroscopy (XPS) experiments were performed on the mixtures of Tp-COFs-Mo and the photosensitizer $[Ru(bpy)_3]Cl_2$ to reveal the electron capture capability of the Mo atom in Tp-COFs-Mo during the photocatalytic reaction. As illustrated in Fig. 4e, f and S37, under visible light irradiation, the Mo sites of all three photocatalytic materials captured electrons, while the Ru sites of the photosensitizer lost electrons, verifying the electron transfer pathway from the photosensitizer to the Mo site in Tp-COFs-Mo. The shift magnitude of Mo 3d orbital binding energies in Tp-COFs-Mo decreased in the order TpPa-COF-Mo > TpTa-COF-Mo > TpBd-COF-Mo, which indicated that the Mo atom in TpPa-COF-Mo can capture more electrons under the same irradiation duration. Therefore, it could be inferred that more electrons could be captured by TpPa-COF-Mo with the smallest torsion angle which promoted the accumulation of electrons in the d-orbitals of Mo near the Fermi level, thus resulting in the stronger C–C coupling ability, and thus a higher C_2H_6 production rate.[57,58]

The key intermediates during CO_2 photoreduction to C_2H_6 over TpPa-COF-Mo were captured through *in situ* Fourier transform spectroscopy (FTIR). As displayed in Fig. 5a, the absorption peaks at 1281 and 1432 cm^{-1} were ascribed to the symmetric stretching vibration of $*HCO_3^{2-}$, and the peaks at 1524 and 1359 cm^{-1} were assigned to the symmetric stretching of $*CO_3^{2-}$.[59] Additionally, the characteristic peaks of *CO and *COOH intermediates associated with CO generation were detected at 2098 and 1668 cm^{-1}, respectively.[60,61] Notably, the peaks of *CHO and *CHOCO intermediates were observed at 1717 and 1590 cm^{-1}.[62] which were crucial intermediates in the CO_2 photoreduction to C_2H_6, and the intensities of these peaks gradually increased as the irradiation time was extended.

Based on these intermediates detected by *in situ* FTIR spectroscopy, the Gibbs free energy changes in the CO_2RR to C_2H_6 were acquired by DFT calculations to elucidate the reaction mechanism over TpPa-COF-Mo. Here, we simulated the

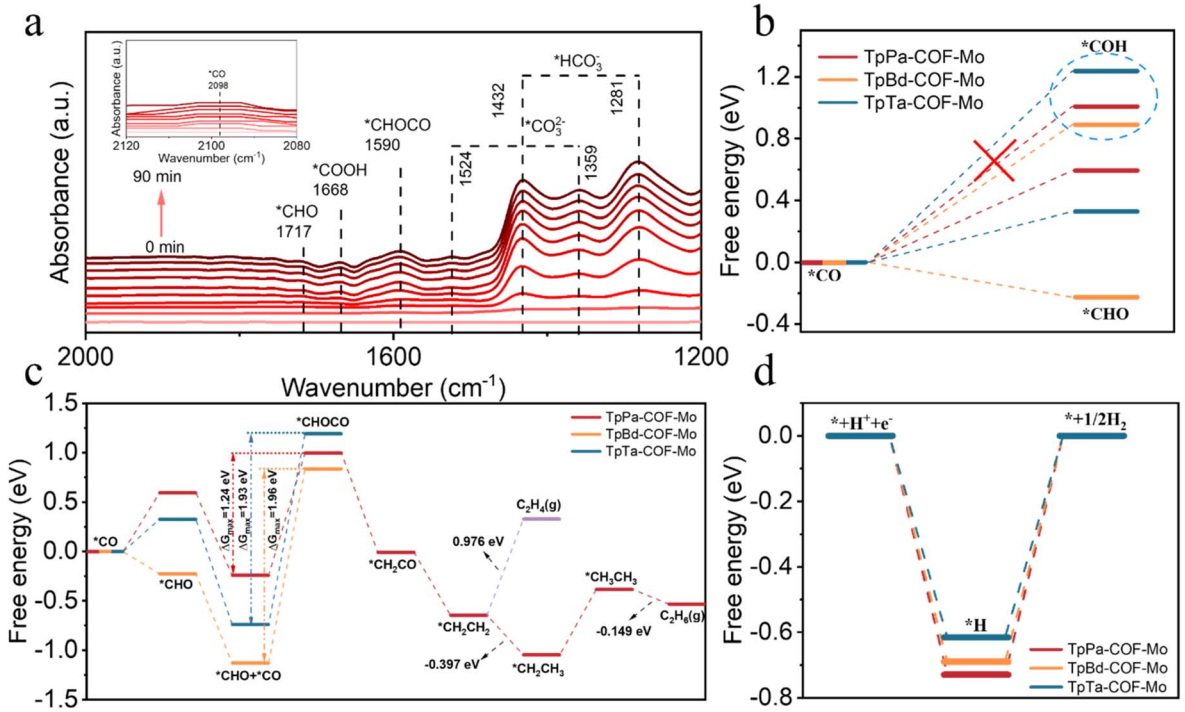

Fig. 5 Mechanism of C–C coupling. (a) *In situ* ATR-FTIR spectra of TpPa-COF-Mo for the detection of intermediates during CO_2 photoreduction. (b) Gibbs free energy diagrams for the conversion of *CO into different intermediates. (c) Gibbs free energy profiles of the CO_2RR to C_2H_6 over Tp-COFs-Mo. (d) Gibbs free energy profiles of the hydrogen evolution reaction over Tp-COFs-Mo.

reaction pathway of the CO_2RR to ethane starting from CO, and focused on the optimal process of C–C coupling of intermediates. First, *CO may be coupled to form *OCCO or hydrogenated to produce *CHO/*COH.[63] As shown in Fig. S38a, the direct C–C coupling of two *CO species at the Mo site of TpPa-COF-Mo to generate the *OCCO intermediate seems infeasible, which means that *CO should preferably undergo the hydrogenation reaction. In this case, the free energy for the hydrogenation of the O atom in *CO to form the *COH intermediate was higher than that for the hydrogenation of the C atom in *CO to produce the *CHO intermediate over Tp-COFs-Mo (Fig. 5b), suggesting that *CHO was more favorable for adsorption and activation on Mo active sites. Therefore, *CO and *CHO intermediates would be coupled to form the *CHOCO intermediate (Fig. S38b). The energy barrier for the formation of the *CHOCO intermediate was the highest in the entire process of the CO_2RR to C_2H_6, and thus this step was identified as the rate-determining step of this reaction. Therefore, despite sufficient light harvesting and improved exciton dissociation or charge transport, the overall efficiency is most likely limited by surface kinetics, particularly the C–C coupling step. Importantly, the energy barrier for the formation of the *CHOCO intermediate over TpPa-COF-Mo (1.24 eV) was lower than that over TpTa-COF-Mo (1.93 eV) and TpBd-COF-Mo (1.96 eV) (Fig. 5c), implying that TpPa-COF-Mo with the smallest torsion angle was conducive to the production of C_2H_6 from a thermodynamic perspective. Moreover, the change in the ΔG value from $*CH_2CH_2$ to $*CH_2CH_3$ (−0.397 eV) was more negative than that for the desorption (0.976 eV) of $*CH_2CH_2$ to produce C_2H_4(g) over TpPa-COF-Mo, demonstrating a more favorable process for ethane production compared to the ethylene pathway.

It is known that the production rate of H_2 significantly affects the selectivity for C_2H_6; therefore, we calculated the ΔG values for *H (active hydrogen) adsorption on the Mo active sites in the COFs, as shown in Fig. 5d. It was found that TpPa-COF-Mo exhibits higher binding ability to *H (−0.729 eV) than TpBd-COF-Mo (−0.689 eV) and TpTa-COF-Mo (−0.616 eV), which remarkably inhibited the production efficiency of H_2 and improves the selectivity of C_2H_6. These results revealed the importance of the torsion angle in Tp-COFs-Mo, and the smallest torsion angle of TpPa-COF-Mo resulted in a reduced interlayer distance and induced Pauli repulsion, which weakened electron distribution in the interlayer region and enhanced that within the layers, thereby facilitating effective electron transfer from the photosensitizer to the Mo site through the faster intralayer pathway and leading to significant electron accumulation at this site. This boosted the adsorption capacity of the Mo site for *H, lowered the energy barrier of *CHOCO formation, inhibited the production of H_2 and efficiently promoted the conversion of CO_2 to C_2H_6. From the above experimental and theoretical results, we propose a detailed mechanism for the photoreduction of CO_2 to C_2H_6 over TpPa-COF-Mo. Under visible light irradiation, the photosensitizer $[Ru(bpy)_3]Cl_2$ is excited to generate electrons, which then migrated to the Mo site. Afterwards, CO_2 is reduced to *CO at the Mo active sites and then *CHOCO intermediates are formed by C–C coupling between *CO and *CHO intermediates. Ultimately, the *CHOCO intermediate is continuously

hydrogenated and deoxidized to C_2H_6. The residual holes are trapped by TEOA, which subsequently undergoes oxidation to form $TEOA_{ox+}$, and the entire cycle is completed.

Conclusions

In summary, we constructed a series of β-ketoenamine-linked Tp-COFs-Mo with different torsion angles but structurally identical Mo–N_3O active sites for photocatalytic the CO_2RR to C_2H_6 production. We found that under visible light irradiation, the production rate of C_2H_6 over TpPa-COF-Mo reached 262.6 μmol g^{-1} h^{-1} with an electron selectivity of 91.8%, which is superior to that of most COF-, POP-, and MOF-based photocatalysts reported in the literature. Theoretical calculations and *in situ* FTIR spectroscopic results revealed that the torsion angle of COFs had an important effect on the transport rate of photogenerated electrons, and a smaller torsion angle led to increased electron accumulation, enhanced adsorption of *H, and a reduced energy barrier of *CHOCO at the Mo sites in TpPa-COF-Mo, thus inhibiting the production of H_2 and boosting the selectivity and production rate of C_2H_6. This work provides a new pathway for the rational regulation of COF photocatalytic performance by using torsion angles to efficiently generate C_2 products with a high production rate and selectivity.

Author contributions

J. J. W., H. Y. W., Q. Z. and Y. M. designed the experiments. Y. M. and S. Q. G. performed the experiments and analysed the data. Y. J. D. and Y. Y. G. completed some synthesis experiments. H. C. provided the DFT calculation support. Y. M., H. Y. W., J. J. W. and Q. Z. wrote the manuscript. All authors discussed the results and commented on the manuscript.

Conflicts of interest

The authors declare no competing interests.

Data availability

The data that support the findings of this study are available in the paper and supplementary information (SI). Source data are provided with this paper. Supplementary information is available. See DOI: https://doi.org/10.1039/d5sc09241h.

Acknowledgements

The authors gratefully acknowledge the financial support from the National Natural Science Foundation of China (No. 22273017, 22233006 and 22408089), the Natural Science Foundation of Henan province (No. 242300421206), the excellent S&T innovation team of Henan Normal University (No. 2022TD06) and the 111 project (No. D17007).

Notes and references

1 S. Heidari, A. R. Shojaei, F. Esmaeilzadeh and D. Mowla, *J. Environ. Chem. Eng.*, 2024, **12**, 114069.
2 S. Yin, Z. Li, Y. Hu, X. Luo and J. Li, *Green Energy Environ.*, 2024, **9**, 1407–1418.
3 Y. Liu, F. Wang, Z. Jiao, S. Bai, H. Qiu and L. Guo, *Electrochem. Energy Rev.*, 2022, **5**, 5.
4 J. Wang, X. Liu, J. Ma, S. Zhang, H. Liu, Y. Dong and Q. Yang, *Green Chem. Eng.*, 2024, **5**, 383–389.
5 Y. Huo, X. Zhou, F. Zhao, C. Ai, Z. Wu, Z. Chang and B. Zhu, *Acta Phys. Chim. Sin.*, 2025, **41**, 100148.
6 Y. Wang, X. Shang, J. Shen, Z. Zhang, D. Wang, J. Lin, J. C. S. Wu, X. Fu, X. Wang and C. Li, *Nat. Commun.*, 2020, **11**, 3043.
7 Z. Jiang, X. Xu, Y. Ma, H. S. Cho, D. Ding, C. Wang, J. Wu, P. Oleynikov, M. Jia, J. Cheng, Y. Zhou, O. Terasaki, T. Peng, L. Zan and H. Deng, *Nature*, 2020, **586**, 549–554.
8 X. Xiong, C. Mao, Z. Yang, Q. Zhang, G. I. N. Waterhouse, L. Gu and T. Zhang, *Adv. Energy Mater.*, 2020, **10**, 2002928.
9 S. Man, W. Jiang, X. Guo, O. Ruzimuradov, S. Mamatkulov, J. Low and Y. Xiong, *Chem. Mater.*, 2024, **36**, 1793–1809.
10 H. Ou, G. Li, W. Ren, B. Pan, G. Luo, Z. Hu, D. Wang and Y. Li, *J. Am. Chem. Soc.*, 2022, **144**, 22075–22082.
11 G. H. Han, J. Bang, G. Park, S. Choe, Y. J. Jang, H. W. Jang, S. Y. Kim and S. H. Ahn, *Small*, 2023, **19**, 2205765.
12 Y. Wu, Z. Li, Q. Chen, Z. Lou, G. Wang and J. Mao, *ACS Catal.*, 2025, **15**, 3558–3569.
13 W. Wang, C. Deng, S. Xie, Y. Li, W. Zhang, H. Sheng, C. Chen and J. Zhao, *J. Am. Chem. Soc.*, 2021, **143**, 2984–2993.
14 S. Xie, W. Ma, X. Wu, H. Zhang, Q. Zhang, Y. Wang and Y. Wang, *Energy Environ. Sci.*, 2021, **14**, 37–89.
15 J. Yang, Z. Chen, L. Zhang and Q. Zhang, *ACS Nano*, 2024, **18**, 21804–21835.
16 B. Mishra, A. Alam, A. Chakraborty, B. Kumbhakar, S. Ghosh, P. Pachfule and A. Thomas, *Adv. Mater.*, 2024, **37**, 2413118.
17 S. Ali, G. Yasin, R. Iqbal, X. Huang, J. Su, S. Ibraheem, Z. Zhang, X. Wu, F. Wahid, P. M. Ismail, L. Qiao and H. Xu, *Mol. Catal.*, 2022, **524**, 112285.
18 R. Iqbal, G. Yasin, M. Hamza, S. Ibraheem, B. Ullah, A. Saleem, S. Ali, S. Hussain, T. Anh Nguyen, Y. Slimani and R. Pathak, *Coord. Chem. Rev.*, 2021, **447**, 214152.
19 J. Li, H. Jin, T. Qin, F. Liu, S. Wu and L. Feng, *ACS Nano*, 2024, **18**, 4539–4550.
20 Y. Liu, Z. Zhao, W. Xu and W. Gong, *Catal. Sci. Technol.*, 2024, **14**, 3211–3218.
21 D. Blätte, F. Ortmann and T. Bein, *J. Am. Chem. Soc.*, 2024, **146**, 32161–32205.
22 S. Seki, R. P. Paitandi, W. Choi, S. Ghosh and T. Tanaka, *Acc. Chem. Res.*, 2024, **57**, 2665–2677.
23 X. Xu, W. Shao, G. Tai, M. Yu, X. Han, J. Han, G. Wu and W. Xing, *Sep. Purif. Technol.*, 2024, **333**, 125890.
24 Z. Liu, Y. Xie, L. Liu, X. Cai, H. Yin, M. Zuo, Y. Liu, S. Feng, W. Huang and D. Wu, *Small*, 2024, **20**, 2309194.

25 S. Wang, X. Liao, D. Cao, C. Huo, Y. Li, J. Wang and H. Jiao, *J. Phys. Chem. C*, 2007, **111**, 16934–16940.
26 W. Li, H. Wang, X. Zheng, L. Ricardez Sandoval, Q. Wu and G. Bai, *Chem. Eng. J.*, 2023, **453**, 139779.
27 B. Hammer and J. K. Norskov, *Nature*, 1995, **376**, 238–240.
28 H. Wang, L. Zhang, K. Wang, X. Sun and W. Wang, *Appl. Catal., B*, 2019, **243**, 771–779.
29 G. Gao, Q. Wang, P. Zhu, H. Zhu, Y. Qu and G. Wang, *J. Mater. Chem. A*, 2022, **10**, 13393–13401.
30 R. Zhang, P. Li, F. Wang, L. Ye, A. Gaur, Z. Huang, Z. Zhao, Y. Bai and Y. Zhou, *Appl. Catal., B*, 2019, **250**, 273–279.
31 M. Kou, W. Liu, Y. Wang, J. Huang, Y. Chen, Y. Zhou, Y. Chen, M. Ma, K. Lei, H. Xie, P. K. Wong and L. Ye, *Appl. Catal., B*, 2021, **291**, 120146.
32 Q. Zhang, S. Gao, X. Zhao, H. Wang, Y. Guo, Z. Liu and J. Wang, *Chem. Sci.*, 2025, **15**, 15166–15176.
33 N. Das, R. Paul, R. Chatterjee, D. B. Shinde, Z. Lai, A. Bhaumik and J. Mondal, *Chem.–Asian J.*, 2023, **18**, e202200970.
34 L. Liang, Y. Wang, W. Ren, X. Gao, L. Zheng and F. Lu, *ACS Appl. Polym. Mater.*, 2023, **5**, 9477–9488.
35 S. Ghosh, A. Nakada, M. A. Springer, T. Kawaguchi, K. Suzuki, H. Kaji, I. Baburin, A. Kuc, T. Heine, H. Suzuki, R. Abe and S. Seki, *J. Am. Chem. Soc.*, 2020, **142**, 9752–9762.
36 C. Qin, Y. Yang, X. Wu, L. Chen, Z. Liu, L. Tang, L. Lyu, D. Huang, D. Wang, C. Zhang, X. Yuan, W. Liu and H. Wang, *Nat. Commun.*, 2023, **14**, 6740.
37 Q. Zhang, S. Gao, Y. Guo, H. Wang, J. Wei, X. Su, H. Zhang, Z. Liu and J. Wang, *Nat. Commun.*, 2023, **14**, 1147.
38 Z. Chen, J. Guo, F.-H. Song, S.-D. Wang, S. A. C. Carabineiro, S.-X. Ouyang and L.-L. Wen, *ACS Catal.*, 2025, **15**, 8284–8296.
39 J. Zhang, Y. Cao, W. Liu, T. Cao, J. Qian, J. Wang, X. Yao, A. Iqbal and W. Qin, *ChemSusChem*, 2022, **15**, e202101510.
40 C. Janiak, *J. Chem. Soc., Dalton Trans.*, 2000, 3885–3896, DOI: 10.1039/B003010O.
41 R. Ma, Y. Zhang, F. Yu, S. Wei, Y. Xing, C. Qiao, Z. Xia, Q. Yang, G. Xie and S. Chen, *ACS Catal.*, 2025, **15**, 3046–3060.
42 Y. Yang, Y. Lu, H. Zhang, Y. Wang, H. Tang, X. Sun, G. Zhang and F. Zhang, *ACS Sustainable Chem. Eng.*, 2021, **9**, 13376–13384.
43 K. Dey, S. H. Kunjattu, A. M. Chahande and R. Banerjee, *Angew. Chem., Int. Ed.*, 2020, **59**, 1161–1165.
44 L. Yin, Y. Zhao, Y. Xing, H. Tan, Z. Lang, W. Ho, Y. Wang and Y. Li, *Chem. Eng. J.*, 2021, **419**, 129984.
45 X. Li, G. Zhang, Y. Chang, Q. Cui, M. Zhang, W. Zou and M. Zhou, *Chem. Eng. J.*, 2024, **499**, 156337.
46 P. Du, K. Hu, J. Lyu, H. Li, X. Lin, G. Xie, X. Liu, Y. Ito and H. Qiu, *Appl. Catal., B*, 2020, **276**, 119172.
47 H. Yang, M. Luo, S. Lu, Q. Zhang, Y. Chao, F. Lv, L. Zhu, L. Bai, L. Yang, W. Wang, D. Wei, Y. Liang, L. Gu, H. Chen and S. Guo, *Chem*, 2022, **8**, 2460–2471.
48 S. Guo, X. Qi, H. Zhou, J. Zhou, X. Wang, M. Dong, X. Zhao, C. Sun, X. Wang and Z. Su, *J. Mater. Chem. A*, 2020, **8**, 11712–11718.
49 S. Yu, X. Gao, J. Wang, W. Sun and Y. Li, *Nanoscale*, 2025, **17**, 27172–27199.
50 H. C. Woo, J. W. Choi, J. Shin, S. Chin, M. H. Ann and C. L. Lee, *J. Phys. Chem. Lett.*, 2018, **9**, 4066–4074.
51 Y. Zhang, Y. Liu, H. Li, G. Bai and X. Lan, *Chem. Eng. J.*, 2024, **489**, 151479.
52 F. Liu, P. Zhou, Y. Hou, H. Tan, Y. Liang, J. Liang, Q. Zhang, S. Guo, M. Tong and J. Ni, *Nat. Commun.*, 2023, **14**, 4344.
53 M. Dong, W. Li, J. Zhou, S. You, C. Sun, X. Yao, C. Qin, X. Wang and Z. Su, *Chin. J. Catal.*, 2022, **40**, 2678–2684.
54 X. Wang, C. Zhang, R. Bi, Z. Peng, A. Song, R. Zhang, H. He, J. Qi, J. Gong, C. Niu, R. Liang and J. Qiu, *Adv. Funct. Mater.*, 2025, **35**, 2421623.
55 H. Li, Z. Luo, J. Han, Z. Yu, Q. Xue, Y. Zhao, J. Du, X. Zhou and F. Wang, *Angew. Chem., Int. Ed.*, 2026, **65**, e24704.
56 H. Peng, Y. Liu, Y. Wang, M. Song, H. Song, P. Chen and S. Yin, *ACS Catal.*, 2024, **14**, 2971–2980.
57 S. Chen, F. Huang, L. Mao, Z. Zhang, H. Lin, Q. Yan, X. Lu and J. Shi, *Nano-Micro Lett.*, 2024, **17**, 32.
58 X. Zhu, X. Yuan, M. Ge and Y. Tang, *Small*, 2024, **20**, 2405158.
59 J. Ji, R. Li, H. Zhang, Y. Duan, Q. Liu, H. Wang and Z. Shen, *Appl. Catal., B*, 2023, **321**, 122020.
60 B. Wang, W. Zhang, G. Liu, H. Chen, Y. Weng, H. Li, P. K. Chu and J. Xia, *Adv. Funct. Mater.*, 2022, **32**, 2202885.
61 J. Wang, C. Yang, L. Mao, X. Cai, Z. Geng, H. Zhang, J. Zhang, X. Tan, J. Ye and T. Yu, *Adv. Funct. Mater.*, 2023, **33**, 2213901.
62 R. Xu, D. Si, S. Zhao, Q. Wu, X. Wang, T. Liu, H. Zhao, R. Cao and Y. Huang, *J. Am. Chem. Soc.*, 2023, **145**, 8261–8270.
63 X. Yang, L. Ren, Z. Chen, H. Li and Y. Yuan, *Adv. Mater.*, 2025, **37**, 2412299.